nature biotechnology

ARTICLES

https://doi.org/10.1038/s41587-021-01026-y

Deletion and replacement of long genomic sequences using prime editing

Tingting Jiang[1], Xiao-Ou Zhang[2,3], Zhiping Weng[2] and Wen Xue[1,4,5,6] ✉

Genomic insertions, duplications and insertion/deletions (indels), which account for ~14% of human pathogenic mutations, cannot be accurately or efficiently corrected by current gene-editing methods, especially those that involve larger alterations (>100 base pairs (bp)). Here, we optimize prime editing (PE) tools for creating precise genomic deletions and direct the replacement of a genomic fragment ranging from ~1 kilobases (kb) to ~10 kb with a desired sequence (up to 60 bp) in the absence of an exogenous DNA template. By conjugating Cas9 nuclease to reverse transcriptase (PE-Cas9) and combining it with two PE guide RNAs (pegRNAs) targeting complementary DNA strands, we achieve precise and specific deletion and repair of target sequences via using this PE-Cas9-based deletion and repair (PEDAR) method. PEDAR outperformed other genome-editing methods in a reporter system and at endogenous loci, efficiently creating large and precise genomic alterations. In a mouse model of tyrosinemia, PEDAR removed a 1.38-kb pathogenic insertion within the *Fah* gene and precisely repaired the deletion junction to restore FAH expression in liver.

Genetic insertions, duplications and indels account for ~14% of 60,008 known human pathogenic variants[1] (Fig. 1a). Many of these abnormal insertions and duplications involve larger DNA fragments (>100 bp). Indeed, retrotransposon element insertions, ranging from 163 to 6,000 bp (refs. [2,3]), disrupt the normal expression and function of genes[4], thereby causing genetic diseases, such as cystic fibrosis, hemophilia A, X-linked dystonia-parkinsonism and inherited cancers[4–7]. Precise genome-editing technologies that simultaneously delete the inserted or duplicated DNA sequences and repair the disrupted genomic site might provide a way to treat a wide range of diseases.

The CRISPR/Cas9 system is a powerful gene-editing tool for correcting pervasive pathogenic gene mutations. Using dual single guide RNAs (sgRNAs), Cas9 can induce two double-strand breaks (DSBs). The two cut ends are then ligated through the non-homologous end joining (NHEJ) repair pathway, leading to a ≤5-Mb target fragment deletion in vitro[8,9] and in vivo[10–12]. However, the random indels generated by NHEJ lower the editing accuracy of this method. When a donor DNA template is present, CRISPR/Cas9 can insert a desired sequence at the cut site to more accurately repair the deletion junction through homology-directed repair (HDR)[13,14]. Nevertheless, the repair efficiency of CRISPR-mediated HDR is hindered by the exogenous DNA donor and is limited in postmitotic cells[15,16]. To further expand the gene-editing toolbox, a novel CRISPR-associated gene editor, called PE[17], was developed by conjugating an engineered reverse transcriptase (RT) to a catalytically impaired Cas9 'nickase' ($Cas9^{H840A}$) that cleaves only one DNA strand. An extension at the 3′ end of the pegRNA functions as an RT template, allowing the nicked site to be precisely repaired[17,18]. Thus, PE can mediate small deletions, insertions and base editing without creating DSBs or requiring donor DNA[17] and holds great promise for correcting human genetic diseases[19–22]. Yet, PE has not been applied to delete larger DNA fragments. Here, we engineer the PEDAR method, enabling accurate deletion of a larger genomic fragment and concurrent insertion of a desired sequence without requiring a repair template.

Results

PEDAR strategy. To achieve accurate and efficient large-fragment deletion and simultaneous insertion without requiring a DNA template (Supplementary Fig. 1a), we modified the PE system to use a pair of pegRNAs (hereafter referred to as pegF and pegR) rather than one pegRNA and one nicking guide RNA. We reasoned that using two pegRNAs would enable concurrent targeting of both DNA strands. The 3′ extension of each pegRNA is a reverse complementary RT template that encodes the sequences for desired insertion. In theory, this newly engineered system could mediate accurate deletion–repair through the following steps (Fig. 1b, left): (1) prime editor recognizes the 'NGG' protospacer adjacent motif (PAM) sequence, binds and nicks the two complementary strands of DNA on either side of the large fragment[8], (2) the desired insertion sequences are reverse transcribed into the target site using the RT template linked to the pegRNAs, (3) the complementary DNA strands containing the edits are annealed, (4) the original DNA strands (that is, 5′ flaps) are excised and (5) DNA is repaired. However, Cas9 nickase cannot effectively mediate larger target deletions with paired guide RNAs[23,24]. Indeed, PE applications reported in the literature are limited to programming deletions of less than 100 bp, raising the concern that PE cannot generate long genomic deletions[18].

Fully active Cas9 nuclease has been used to program larger deletions with dual sgRNAs[14]. Therefore, we conjugated an active Cas9 nuclease, instead of Cas9 nickase, to the RT[17] to create 'PE-Cas9' (Supplementary Fig. 1b). With a single pegRNA[17], PE-Cas9 and PE generated similar rates of a 3-bp CTT insertion at the cut/nicking site of an endogenous locus (Supplementary Fig. 1c), indicating

[1]RNA Therapeutics Institute, University of Massachusetts Medical School, Worcester, MA, USA. [2]Program in Bioinformatics and Integrative Biology, University of Massachusetts Medical School, Worcester, MA, USA. [3]School of Life Sciences and Technology, Tongji University, Shanghai, China. [4]Department of Molecular, Cell and Cancer Biology, University of Massachusetts Medical School, Worcester, MA, USA. [5]Department of Molecular Medicine, University of Massachusetts Medical School, Worcester, MA, USA. [6]Li Weibo Institute for Rare Diseases Research, University of Massachusetts Medical School, Worcester, MA, USA. ✉e-mail: wen.xue@umassmed.edu

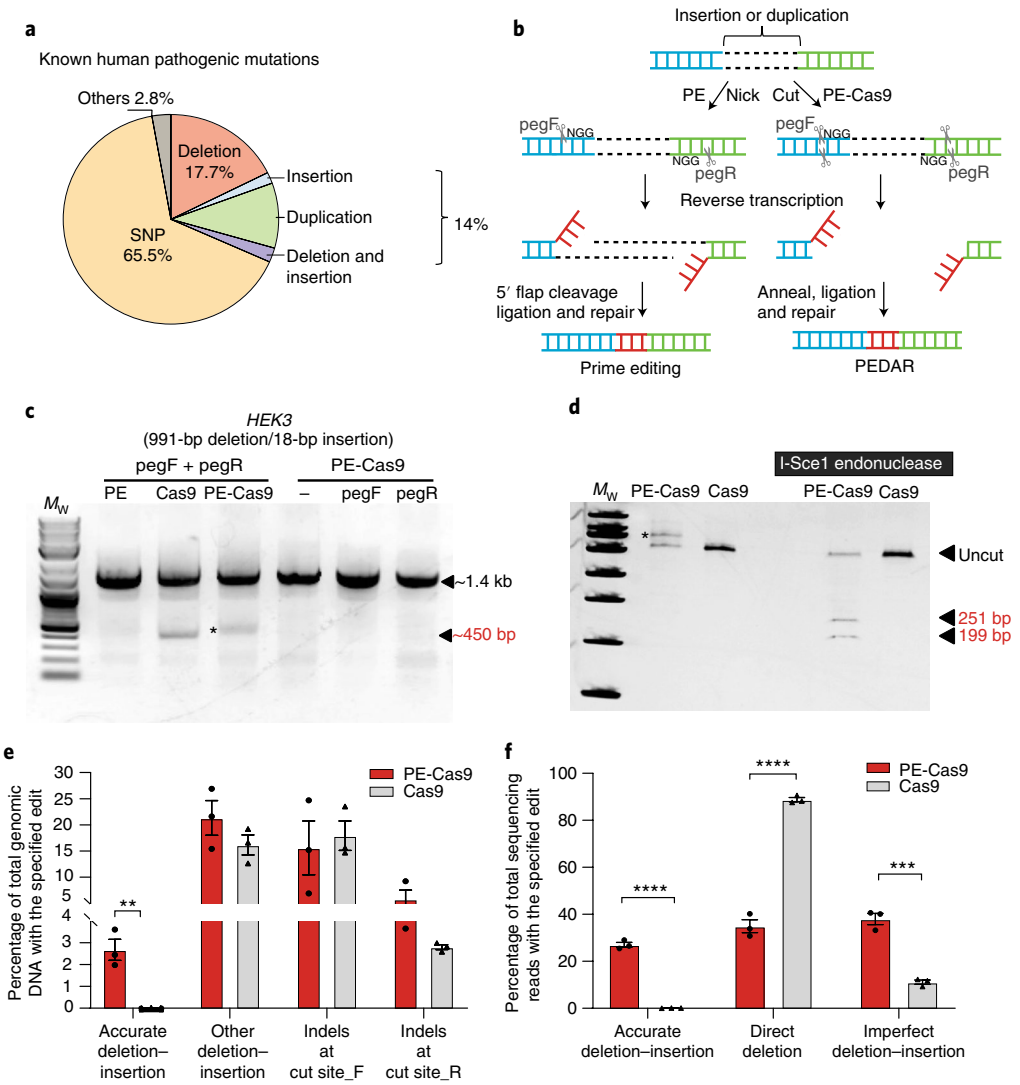

Fig. 1 | PEDAR mediates large target deletion and simultaneous insertion at an endogenous genomic locus. a, Classification of the 60,008 known human pathogenic genetic variants reported in the ClinVar database[1]; SNP, single-nucleotide polymorphism. **b**, Overview of using PE (left) and PEDAR (right) to generate accurate deletion–insertion. The paired pegRNAs targeting the complementary DNA strand are denoted as pegF and pegR. **c**, Deletion of a 991-bp DNA fragment and simultaneous insertion of I-SceI recognition sequence (18 bp) at the *HEK3* locus (chromosome 9:107,422,166–107,423,588). The target genomic region was amplified using primers that span the cut sites. HEK293T cells were transfected with PE, Cas9 or PE-Cas9 with or without single or paired pegRNAs. The ~450-bp band is the expected deletion amplicon (denoted with an asterisk (*)), and the ~1.4-kb band is the amplicon without deletion. **d**, Deletion amplicons from Cas9- or PE-Cas9-treated groups shown in **c** were incubated with or without I-SceI endonuclease and analyzed on a 4–20% TBE gel. Digested products are marked by arrows with expected sizes. The original amplicon is marked as 'Uncut'. The band with insertion of I-SceI recognition sequence is denoted with an asterisk (*). **e**, PE-Cas9- or Cas9-mediated absolute rates of all the editing events in total genomic DNA at the *HEK3* site. Data are represented as mean ± s.e.m. ($n = 3$ biologically independent samples); $^{**}P = 0.0053$, two-tailed *t*-test. **f**, Deep sequencing of deletion amplicons shown in **c**. Bar chart shows distribution of all deletion events, including accurate deletion–insertion, direct deletion (deletion without any insertions) or imperfect deletion–insertion. Editing rate represents the reads with indicated editing/total deletion events. Data are represented as mean ± s.e.m. ($n = 3$ biologically independent samples); $^{****}P = 0.0000140$; $^{***}P = 0.002$, two-tailed *t*-test.

that Cas9 nuclease activity does not affect PE efficiency. We hypothesized that, with the guidance of two pegRNAs targeting both complementary strands of DNA, PE-Cas9 can introduce two DSBs and delete the intervening DNA fragment between the two cut sites. Concurrently, the desired edits are incorporated at target sites using the RT template at the 3′ extension of the pegRNAs. The two complementary edits then function as homologous sequences to direct the ligation and repair of the deletion junction. We term this method PEDAR (Fig. 1b, right).

Compare PE, Cas9 and PEDAR in programming deletion–insertion. We compared the efficiency of PEDAR, PE and Cas9 systems in coupling large target deletion and accurate insertion at the endogenous *HEK3* genomic locus in HEK293T cells. We designed two pegRNAs with an offset of 979 bp (distance between the two NGG PAM sequences) to program a 991-bp deletion/18-bp insertion at the *HEK3* site. The RT template at the 3′ extension of the pegRNAs encodes an I-SceI recognition sequence (18 bp), which will be reversed transcribed and integrated into the target site (Supplementary Fig. 1d). Paired pegRNAs along with PE, PE-Cas9 or Cas9 were transfected into cells. Delivery of PE-Cas9 with or without single pegRNA was used as a negative control. Three days after transfection, we amplified the target genomic site and found that treatment with either PE-Cas9 or active Cas9, but not

PE, led to a ~450-bp deletion amplicon. This amplicon was ~1 kb shorter than the amplicon without deletion (Fig. 1c). We digested the deletion amplicon with I-SceI endonuclease and observed that only the PE-Cas9-treated group showed cut bands of expected size (~251 bp and ~199 bp), indicating insertion of the I-SceI recognition sequence (Fig. 1d). Using real-time quantitative PCR (qPCR), we found that PE-Cas9 generates an accurate deletion–insertion frequency of 2.67 ± 0.839% in total genomic DNA, whereas Cas9 seldom generated accurate editing (0.0112 ± 0.00717%; Fig. 1e). To further verify editing accuracy, we purified the deletion amplicon (~450-bp band in Fig.1c) and performed a deep sequencing analysis. We found that PE-Cas9 mediates 27.0 ± 1.83% accurate editing of total deletion events (Fig. 1f). Taken together, our findings suggest that PEDAR outperforms PE and Cas9 editing in programming accurate large-fragment deletion and simultaneous insertion.

PEDAR also generated unintended edits, which are classified as (1) other deletion–insertion, including direct deletion without insertion and imperfect deletion–insertion, and (2) small indels generated by individual pegRNA at the two cut sites, hereafter referred to as cut site_F and cut site_R. We measured the incidence of these events in total genomic DNA by qPCR and observed that PE-Cas9 and Cas9 generated comparable rates of unintended edits (Fig. 1e). Of all the deletion events, PE-Cas9 generated 38.0 ± 4.15% imperfect deletion–insertions caused by imprecise DNA repair or pegRNA scaffold insertion[17] and a much lower rate of direct deletion without insertion than that mediated by active Cas9 (35.0 ± 4.80% and 88.8 ± 1.58%, respectively) (Fig. 1f). PE-Cas9-mediated unintended deletion edits with the highest sequencing reads are listed in Supplementary Fig. 2a and Supplementary Table 3. PE-Cas9 or Cas9 also introduced indels at the two cut sites without generating the desired deletion. Sanger sequencing of the amplicon without deletion (~1.4-kb band in Fig. 1c) revealed no substantial difference in small indels caused by PE-Cas9 and Cas9 (Supplementary Fig. 2b).

To explore the potential repair mechanism underlying PEDAR-mediated editing, we delivered PE-Cas9 with one pegRNA and one sgRNA targeting the *HEK3* locus into cells. PE-Cas9 with paired pegRNAs served as a positive control (Supplementary Fig. 2c). Although PE-Cas9 generated a ~450-bp deletion amplicon using one pegRNA and one sgRNA (Supplementary Fig. 2d), this amplicon failed to be digested into two distinct bands by I-Sce1 endonuclease (Supplementary Fig. 2e). Deep sequencing revealed minimal accurate deletion–insertion (0.716 ± 0.0868%) in the cells transfected with one pegRNA and one sgRNA as compared to a 26.5 ± 1.12% accurate editing rate in cells treated with PEDAR (Supplementary Fig. 2f). This result demonstrates that the reverse complementary sequences introduced by paired pegRNAs at the two cut sites are essential for directing accurate repair, resembling the annealing and ligation process in microhomology-mediated end joining (MMEJ) or in the single strand annealing (SSA) repair pathway[25,26].

We also investigated how design of the pegRNAs, namely the length of the primer-binding site (PBS) and the design of RT template, might affect editing efficiency of PEDAR. Our original PEDAR system used paired pegRNAs with 13-nucleotide (nt) PBSs. We designed two additional paired pegRNAs with 10-nt or 25-nt PBSs targeting the *HEK3* locus as comparisons. Although all paired pegRNAs supported a ~1-kb deletion (Supplementary Fig. 3a) and simultaneous insertion of the I-Sce1 recognition sequence (Supplementary Fig. 3b), the shorter and longer PBS lengths substantially impaired the accurate editing rate identified by deep sequencing (Supplementary Fig. 3c). To determine the effect of RT template design on editing efficiency, we designed an alternative pegRNA (pegRNA_alt), similar to the pegRNA used in PE2 (ref. [17]), by extending the RT template with a 14-nt sequence homologous to the region after the other cut site (Supplementary Fig. 3d). After transfecting the newly designed paired pegRNAs with PE or PE-Cas9 into cells, we identified a deletion amplicon of the expected size (Supplementary Fig. 3e), and insertion of I-Sce1 recognition sequence was detected in the deletion amplicon (Supplementary Fig. 3f). Deep sequencing of the deletion amplicon revealed that pegRNA_alt notably decreased the PE-Cas9-mediated accurate editing rate compared to the original pegRNAs (Supplementary Fig. 3g). Surprisingly, cotransfection of PE and pegRNA_alt greatly improved the purity of deletion product (85.9 ± 0.644% accurate editing in deletion amplicon; Supplementary Fig. 3g). However, the absolute accurate editing rate in total genomic DNA was comparable between PE/pegRNA_alt and PE-Cas9/pegRNA groups (Supplementary Fig. 3h), potentially due to the limited ability of Cas9 nickase to introduce larger deletions[23,24]. Based on the collective findings, we elected to use pegRNAs with a 13-nt PBS and an RT template without adding the sequence homologous to the target site after incision in the subsequent studies.

To assess the efficiency of PEDAR-mediated deletion–insertion at an endogenous locus other than the *HEK3* site, we targeted the *DYRK1A* locus for deleting a 995-bp DNA fragment and simultaneously inserting I-Sce1 recognition sequence. Treatment of HEK293T cells with PEDAR lead to a ~507-bp deletion band (Supplementary Fig. 4a), and this amplified product could be digested by I-Sce1 endonuclease (Supplementary Fig. 4b). Deep sequencing of the deletion amplicon identified a 2.18 ± 0.552% accurate editing efficiency (Supplementary Fig. 4c). We reasoned that the low GC content at the primer-binding sequences of the two pegRNAs targeting the *DYRK1A* locus (23% of pegF and 31% of pegR) restricted integration of the desired DNA fragment, which is consistent with a report showing poor PE efficiency when the GC content in the PBS is less than 30% (ref. [27]).

PEDAR enables larger deletion and insertion. To further understand the robustness of the PEDAR system, we explored its limits with respect to insertion size and deletion size. First, we set out to insert the I-Sce1 recognition sequence together with either a Flag

Fig. 2 | Flexibility of PEDAR in programming a larger deletion and insertion in HEK293T cells. a, Insert DNA fragments of variable lengths (18 bp, 44 bp and 60 bp) to the target site at the *HEK3* locus. pegRNAs and primers for amplifying the target site are as shown. The expected sizes of digestion products after I-Sce1 treatment are shown. **b**, Amplification of target genomic region using primers spanning the cut sites at the *HEK3* locus. The deletion amplicons are denoted with an asterisk (*). Cells transfected with PE-Cas9 alone serve as negative control. **c**, Deletion amplicons from groups shown in **b** were incubated with or without I-SceI endonuclease and were analyzed in 4–20% TBE gels. Digested products are marked by arrows with expected sizes. The original amplicon is marked as 'Uncut'. **d**, Deep sequencing of deletion amplicons shown in **b**. Bar chart shows accurate deletion–insertion rate. Data represent mean ± s.e.m. ($n = 3$ biologically independent samples); $^{**}P = 0.0024$, two-tailed t-test. **e**, Efficiency of PEDAR in mediating larger deletions. Paired pegRNAs spaced ~8 kb (pegF + pegR1) or 10 kb (pegF + pegR2) apart were designed as indicated to target the *CDC42* locus. Primers used to amplify the target genomic regions are as marked (P1 + P3 and P2 + P4). **f**, The target genomic region was amplified using the primers indicated in **e**. Cells transfected with PE-Cas9 alone served as a negative control. The deletion amplicons are marked with expected sizes (denoted with an asterisk (*)). **g**, Deletion amplicons from Cas9- or PE-Cas9-treated groups shown in **f** were incubated with or without I-SceI endonuclease and were analyzed in 4–20% TBE gels. Digested products are marked with expected sizes. The original amplicon is marked as 'Uncut'. **h**, Deep sequencing of deletion amplicons shown in **f**. Bar chart shows the rate of accurate deletion–insertion events. Data are represented as mean ± s.e.m. ($n = 3$ biologically independent samples).

epitope tag (44 bp total) or a Cre recombinase *loxP* site (60 bp total) into the *HEK3* locus after deletion of a ~1-kb DNA fragment. Two paired pegRNAs were designed with either a 44-nt RT template or a 60-nt RT template, and the pegRNAs with an 18-nt RT template served for comparison (Fig. 2a). For all paired pegRNAs, PE-Cas9 generated the expected deletion (Fig. 2b) and inserted the desired sequence (Fig. 2c) at the target site in cells. Deep sequencing revealed 13.7 ± 1.51% (44-bp insertion) and 12.4 ± 2.88% (60-bp insertion) accurate deletion–insertion rates within total deletion edits, which are substantially lower than the 22.6 ± 0.267% accurate editing efficiency of PE-Cas9 when inserting a shorter sequence (18 bp) (Fig. 2d). To investigate the maximum deletion size generated by PEDAR, we designed two distinct paired pegRNAs with an offset of ~8 kb or ~10 kb to target the *CDC42* locus (Fig. 2e). Using the indicated primers to amplify the corresponding target site, we observed the expected deletion amplicon (Fig. 2f). After I-Sce1 endonuclease

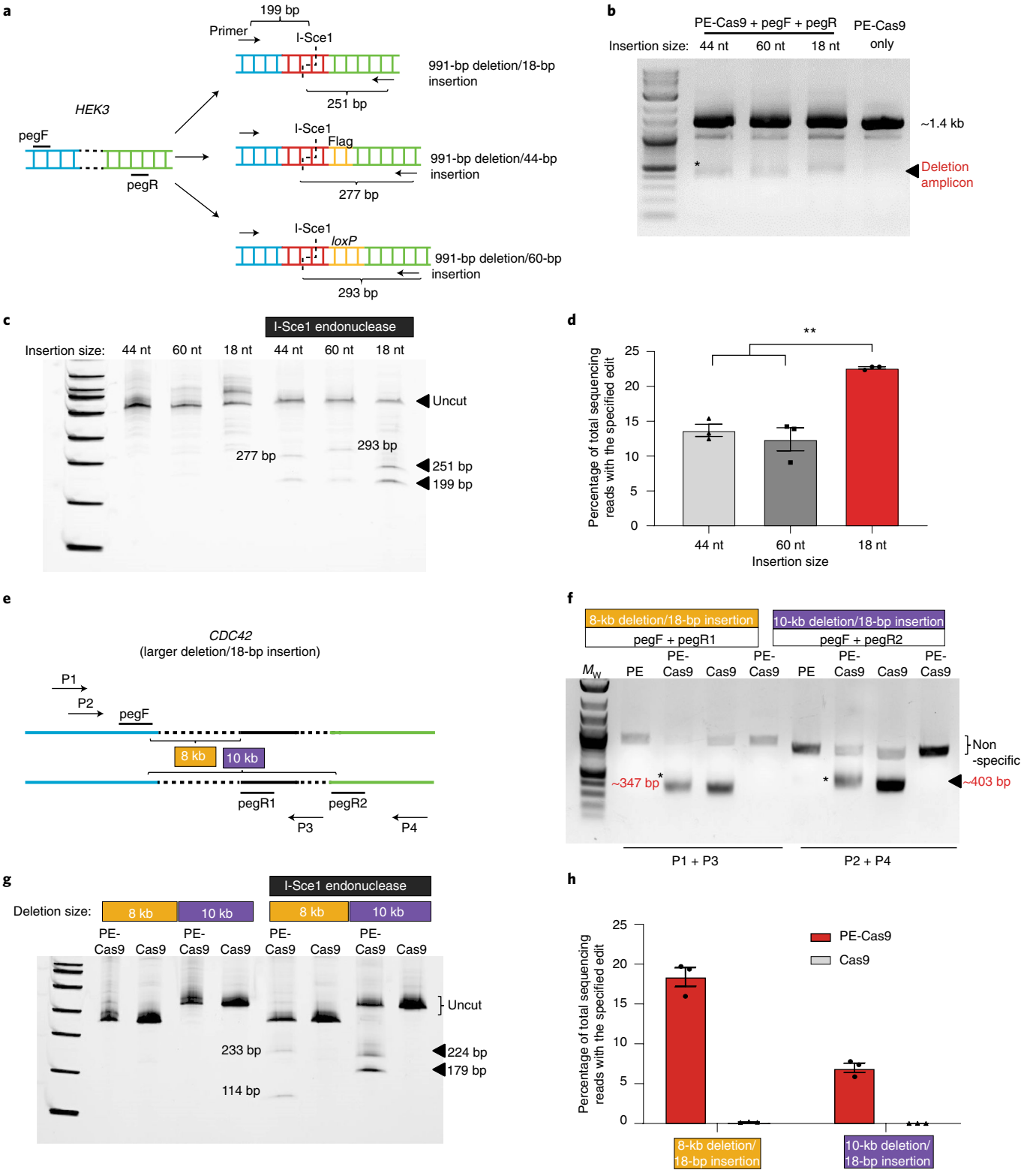

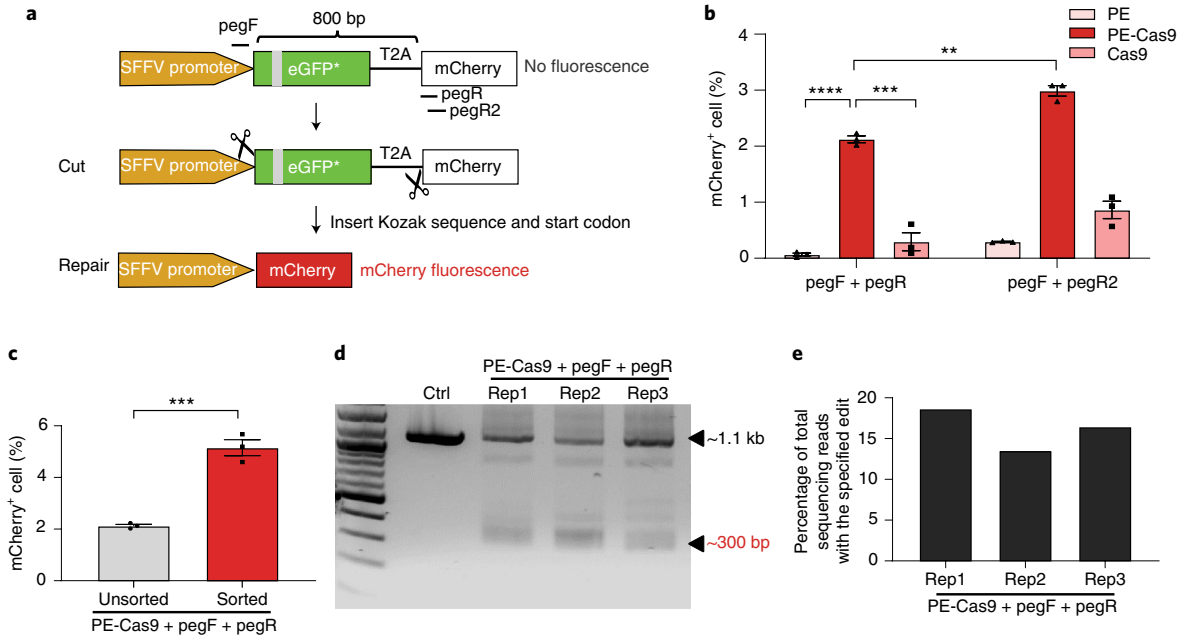

Fig. 3 | PEDAR generates an in-frame deletion to restore mCherry expression in TLR cells. a, Diagram of the TLR system. GFP sequence is disrupted by an insertion (gray). Deleting the disrupted GFP sequence and inserting Kozak sequence and start codon will restore mCherry protein expression; SFFV, spleen focus forming virus. **b**, TLR cells transfected with the indicated paired pegRNAs along with PE, PE-Cas9 or Cas9 were analyzed by flow cytometry, and the percentage of mCherry$^+$ cells are shown among different groups. Data are presented as mean ± s.e.m. ($n = 3$ biologically independent samples); $^{****}P = 0.00000636$; $^{***}P = 0.0004$; $^{**}P = 0.0015$, two-tailed t-test. The asterisk next to eGFP indicates a disrupted eGFP sequence. **c**, mCherry$^+$ cell rate before and after sorting of cells with high transfection levels. A plasmid expressing GFP was cotransfected with paired pegRNAs and PE-Cas9 into TLR cells. Three days later, cells with high GFP expression were selected for analyzing mCherry signal by flow cytometry. Data are presented as mean ± s.e.m. ($n = 3$ biologically independent samples); $^{***}P = 0.0007$, two-tailed t-test. **d**, TLR cells edited by PEDAR were selected by flow cytometry (for mCherry signal) and subjected to PCR amplification using primers spanning the two cut sites. The amplicon with the desired deletion is ~300 bp compared to a ~1.1-kb PCR product in the control group; Rep, replicate; Ctrl, untreated TLR cells. **e**, Efficiency of accurate deletion–insertion in three PEDAR-edited replicates (Reps 1–3) measured by deep sequencing of the deletion amplicons shown in **d**.

treatment, two digested bands were detected in the PE-Cas9-treated group (Fig. 2g). Deep sequencing revealed 18.4 ± 2.07% (8-kb deletion/18-bp insertion) and 6.97 ± 1.00% (10-kb deletion/18-bp insertion) accurate deletion–insertion rates within the deletion amplicon (Fig. 2h). In all, these data demonstrate the robustness and flexibility of PE-Cas9 in generating >10-kb larger deletions and up to 60-bp insertions.

PEDAR restores gene expression by programming in-frame deletion. Next, we asked whether PEDAR could generate large in-frame deletions and accurately repair genomic coding regions to restore gene expression. To answer this question, we used a HEK293T traffic light reporter (TLR) cell line[28,29], which contains a green fluorescent protein (GFP) sequence with an insertion and an mCherry sequence separated by a T2A (2A self-cleaving peptides) sequence. The disrupted GFP sequence causes a frameshift that prevents mCherry expression (Fig. 3a). We hypothesized that PEDAR could restore mCherry signal by accurately deleting the disrupted GFP and T2A sequence (~800 bp in length). We designed two pegRNAs targeting the promoter region before the start codon of GFP and the site immediately after T2A, respectively. In this approach, part of the Kozak sequence and start codon are unintentionally deleted due to the restriction of the PAM sequence. However, we designed the RT template at the 3′ end of pegRNAs to encode the Kozak sequence and start codon to ensure their insertion into the target site by reverse transcription (Fig. 3a).

We treated TLR cells with dual pegRNAs (pegF + pegR) and either PE-Cas9, PE or Cas9 and used flow cytometry to assess the mCherry signal. The frequency of mCherry$^+$ cells was notably higher in the PE-Cas9-treated group (2.12 ± 0.105%) than in the PE- or Cas9-treated groups (Fig. 3b and Supplementary Fig. 5a,b). The mCherry$^+$ cell rate was limited in all three replicates, likely because the cleavage efficiency of pegRNA at cut site_R (pegR) is very low (~1.8%; Supplementary Fig. 5c). Thus, we designed another pegRNA (pegR2) with a ~10.3% cleavage rate (Fig. 3a and Supplementary Fig. 5c) and assessed its efficiency in restoring mCherry expression. Indeed, the newly designed paired pegRNAs greatly improved the mCherry$^+$ cell rate (2.99 ± 0.166%; Fig. 3b and Supplementary Fig. 5d). Alternatively, to enhance the editing rate, we explored the possibility of improving the expression level of gene-editing agents in cells[30]. Cotransfection of cells with a fluorescent protein-expressing plasmid, followed by fluorescence-activated cell sorting (FACS), would enrich for cells with high levels of transgene expression[31,32]. Thus, a GFP-expressing plasmid was cotransfected with PE-Cas9 and paired pegRNAs into TLR cells as an indicator of transfection efficiency. We observed a ~1.42-fold increase in the mCherry$^+$ cell rate after selection of cells with high GFP expression (Fig. 3c and Supplementary Fig. 5e). These results indicate that the editing efficiency of PEDAR largely relies on the efficiency of pegRNA and the expression level of gene-editing components. To verify that PEDAR restored mCherry expression via accurate deletion–insertion, we sorted mCherry$^+$ cells in PE-Cas9-treated groups and amplified the target sequence. In all three replicates, we detected a deletion amplicon that is ~800 bp shorter than the amplicon in untreated control cells (Fig. 3d). Further, we assessed the accurate editing rate by deep sequencing analysis of the ~300-bp deletion amplicon. The results revealed a 16.2 ± 2.58% accurate deletion–insertion rate (Fig. 3e). The most common imperfect editing event across the three

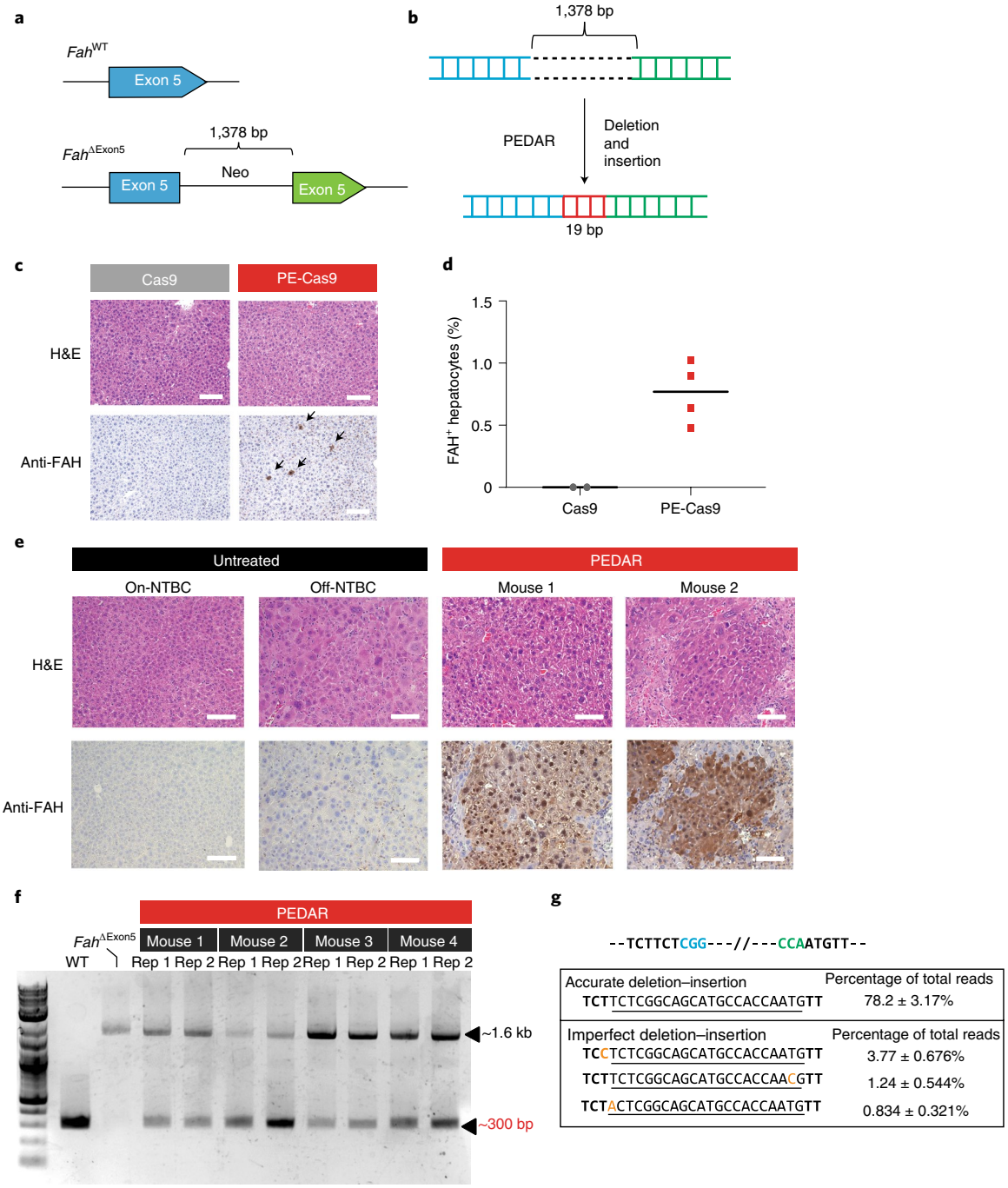

Fig. 4 | PEDAR corrects the pathogenic insertion in a tyrosinemia I mouse model. a, The tyrosinemia I mouse model, referred to as *Fah*$^{\Delta Exon5}$, was derived by integrating a ~1.38-kb neo expression cassette at exon 5 of the *Fah* gene; WT, wild-type. **b**, Diagram showing the application of PEDAR to delete the ~1.38-kb insertion and concurrently repair the target region by inserting a 19-bp DNA fragment (marked in red). **c**, Immunohistochemistry staining and hematoxylin and eosin staining (H&E) of mouse liver sections 7 d after injection of dual pegRNAs with Cas9 or PE-Cas9. FAH$^+$ hepatocytes are indicated by arrows; scale bar, 100 μm. **d**, Quantification of FAH-expressing hepatocytes shown in **c**; $n = 2$, Cas9-treated group; $n = 4$, PE-Cas9-treated group. **e**, Immunohistochemistry and H&E staining of mouse liver sections 40 d after injection of PE-Cas9 with dual pegRNAs. Mice ($n = 4$) were kept off NTBC. Mouse 1 and mouse 2 denote two representative mice from the treatment group. The liver sections from untreated *Fah*$^{\Delta Exon5}$ kept on or off NTBC served as negative controls; scale bar, 100 μm. **f**, Amplification of exon 5 of the *Fah* gene from mouse livers 40 d after injection of PE-Cas9 and paired pegRNAs. The corrected amplicon size is around ~300 bp compared to a ~1.6-kb amplicon without deletion. Four mice in the treated group and two liver lobes (denoted as Rep 1 and Rep 2) per mouse were analyzed; WT, wild-type C57BL/6J mouse; *Fah*$^{\Delta Exon5}$, untreated *Fah*$^{\Delta Exon5}$ mouse. **g**, Accurate correction rate and the top three imperfect editing events identified by deep sequencing. Two PAM sequences are in blue and green. The 22-bp intended insertion (19-bp deletion fragment plus a 3-bp unintentionally deleted sequence) is underlined. Mutated nucleotides in imperfect editing sequences are highlighted in yellow. Data are presented as mean ± s.d. ($n = 8$; two liver lobes per mouse; four mice in total).

replicates restores the mCherry open reading frame, but the inserted sequence lacks three nucleotides compared to the intended insertion (Supplementary Fig. 5f). These data demonstrate that PEDAR can repair genomic coding regions that are disrupted by large insertions.

PEDAR corrects the disrupted *Fah* gene in vivo. Furthermore, to test the in vivo application of PEDAR, we utilized a tyrosinemia I mouse model, referred to as *Fah*$^{\Delta Exon5}$. This tyrosinemia I model is derived by replacing a 19-bp sequence with a ~1.3-kb neo expression cassette[33] at exon 5 of the *Fah* gene[34] (Fig. 4a). This insertion disrupts the *Fah* gene, causing FAH protein deficiency and liver damage. To maintain body weight and survival, these mice are given water supplemented with 2-(2-nitro-4-trifluoromethylbenzoyl)-1,3-cyclohexanedione (NTBC), a tyrosine catabolic pathway inhibitor. We hypothesized that PEDAR can correct the causative *Fah*$^{\Delta Exon5}$ mutation by deleting the large insertion and simultaneously inserting the 19-bp fragment back to repair exon 5 (Fig. 4b). We engineered two pegRNAs targeting the genomic region before and after the inserted neo expression cassette, respectively. At the 3′ end of pegRNAs, a 22-bp RT template encoding the deletion fragment (19 bp) plus a 3-bp sequence that is unintentionally deleted by PE-Cas9 was designed. PE-Cas9 and the two pegRNAs were delivered to the livers of mice ($n=4$) via hydrodynamic injection. Mice ($n=2$) treated with Cas9/pegRNAs served as negative controls. Mice were kept on NTBC water after treatment. One week later, the mice were killed, and immunochemical staining with FAH antibody was performed on liver sections. We detected FAH-expressing hepatocytes on PE-Cas9-treated liver sections (Fig. 4c), with a $0.76\pm0.25\%$ correction rate (Fig. 4d). FAH expression was not detected in Cas9-treated mouse liver (Fig. 4c).

Hepatocytes with corrected FAH protein will gain a growth advantage and eventually repopulate the liver[35]. Therefore, we delivered PE-Cas9 and the two pegRNAs via hydrodynamic injection to mice ($n=4$) and subsequently removed the NTBC supplement to allow repopulation. Untreated *Fah*$^{\Delta Exon5}$ mice (on or off NTBC water) were used as controls. Forty days later, widespread FAH patches were observed in PE-Cas9-treated mouse liver sections, and the corrected hepatocytes showed normal morphology (Fig. 4e and Supplementary Fig. 6a). To understand the editing events in mouse liver, we amplified the target site by using PCR primers spanning exon 5 and identified the ~300-bp deletion amplicon in treated mice, indicating deletion of the ~1.3-kb insertion fragment (Fig. 4f). Deep sequencing of the ~300-bp deletion amplicon uncovered that accurate deletion–insertion constitutes $78.2\pm3.17\%$ of total deletion events (Fig. 4g). We reasoned that, in this mouse model, hepatocytes with corrected FAH protein will outgrow cells with unintended editing, imposing a positive selection for desired editing. The average indel rates caused by each pegRNA at the *Fah* locus were 9.6% (cut site_F) and 0.14% (cut site_R) (Supplementary Fig. 6b). Although one mouse had a much higher average indel rate (27.7%) at cut site_F (mouse 1 in Supplementary Fig. 6b), it did not negatively affect FAH protein expression (mouse 1 in Fig. 4e). Overall, our data demonstrate the potential of using PEDAR in vivo to repair pathogenic mutations caused by large insertions.

Discussion

Here, we expanded the application scope of PE by developing PEDAR that can correct mutations caused by larger genomic rearrangements. Our PEDAR system is similar to a recently developed paired PE method called PRIME-Del, which can introduce 20- to 700-bp target deletions and up to 30-bp insertions[36]. Compared to PRIME-Del, PEDAR seems to be more error prone, introducing higher fractions of direct deletion and imperfect deletion–insertion (Supplementary Fig. 3g); however, both editors exhibited comparable absolute accurate rates in total genomic DNA (Supplementary Fig. 3h). Importantly, we show that PEDAR is able to introduce >10-kb target deletions and up to 60-bp insertions in cells, both of which are larger than what primer editors can generate[17,36]. Moreover, PEDAR can program target deletion–insertion editing in quiescent hepatocytes in mouse liver, where HDR is not favorable[37].

Despite the relative editing efficiency and accuracy of PE-Cas9 being higher than PE and Cas9, the absolute editing efficiency of PEDAR is limited, possibly due to the cleavage activity, PBS length and RT template length of the paired pegRNAs. Designing and comparing multiple paired pegRNA sequences could improve PEDAR efficiency. PEDAR efficiency is also rendered by imperfect deletion–insertion edits due to partial insertion of pegRNA scaffold sequence[17] (Supplementary Fig. 2a). Optimizing the PE system to eliminate this unintended editing might improve the editing purity of PEDAR. Finally, PEDAR efficiency might be restricted by competition of distinct repair pathways at the DSBs. Given that PEDAR might use a similar mechanism as MMEJ or SSA during repair of the DSB (Supplementary Fig. 2f), the NHEJ pathway and MMEJ or SSA pathway might compete for repairing the DSB introduced by Cas9. Previous reports demonstrated that inhibition of NHEJ could enhance the homology-mediated precise editing rate[38,39], and, thus, this approach might improve the PEDAR editing rate.

Finally, we propose that PEDAR could also be used to correct genome duplications (Supplementary Fig. 7a), which constitute ~10% of all human pathogenic mutations according to the ClinVar database[1]. One such genome duplication of high clinical significance is the trinucleotide CAG repeat expansion in the *HTT* gene, the root cause of Huntington's disease[40]. Future studies should investigate whether PEDAR could accurately remove this expansion to reduce CAG repeat length. Thus, our findings have potential implications for the gene therapy field. The significance of PEDAR also extends to basic biology, where it could be used for protein function studies (Supplementary Fig. 7b). Previous studies introduce in-frame deletions by a 'tiling CRISPR' method to explore the functional domain of specific genomic coding or long non-coding regions[41,42].

Online content

Any methods, additional references, Nature Research reporting summaries, source data, extended data, supplementary information, acknowledgements, peer review information; details of author contributions and competing interests; and statements of data and code availability are available at https://doi.org/10.1038/s41587-021-01026-y.

Received: 31 January 2021; Accepted: 19 July 2021;
Published online: 14 October 2021

References

1. Landrum, M. J. et al. ClinVar: public archive of relationships among sequence variation and human phenotype. *Nucleic Acids Res.* **42**, D980–D985 (2014).
2. Cordaux, R. & Batzer, M. A. The impact of retrotransposons on human genome evolution. *Nat. Rev. Genet.* **10**, 691–703 (2009).
3. Chen, J. M., Stenson, P. D., Cooper, D. N. & Ferec, C. A systematic analysis of LINE-1 endonuclease-dependent retrotranspositional events causing human genetic disease. *Hum. Genet.* **117**, 411–427 (2005).
4. Hancks, D. C. & Kazazian, H. H. Roles for retrotransposon insertions in human disease. *Mob. DNA* **7**, 9 (2016).
5. Wang, L., Norris, E. T. & Jordan, I. K. Human retrotransposon insertion polymorphisms are associated with health and disease via gene regulatory phenotypes. *Front. Microbiol.* **8**, 1418 (2017).
6. Hancks, D. C. & Kazazian, H. H. Jr. Active human retrotransposons: variation and disease. *Curr. Opin. Genet. Dev.* **22**, 191–203 (2012).
7. Qian, Y. et al. Identification of pathogenic retrotransposon insertions in cancer predisposition genes. *Cancer Genet.* **216-217**, 159–169 (2017).
8. Ran, F. A. et al. Double nicking by RNA-guided CRISPR Cas9 for enhanced genome editing specificity. *Cell* **154**, 1380–1389 (2013).

9. Cong, L. et al. Multiplex genome engineering using CRISPR/Cas systems. *Science* **339**, 819–823 (2013).
10. Kato, T. et al. Creation of mutant mice with megabase-sized deletions containing custom-designed breakpoints by means of the CRISPR/Cas9 system. *Sci. Rep.* **7**, 59 (2017).
11. Hara, S. et al. Microinjection-based generation of mutant mice with a double mutation and a 0.5 Mb deletion in their genome by the CRISPR/Cas9 system. *J. Reprod. Dev.* **62**, 531–536 (2016).
12. Wang, L. et al. Large genomic fragment deletion and functional gene cassette knock-in via Cas9 protein mediated genome editing in one-cell rodent embryos. *Sci. Rep.* **5**, 17517 (2015).
13. Yeh, C. D., Richardson, C. D. & Corn, J. E. Advances in genome editing through control of DNA repair pathways. *Nat. Cell Biol.* **21**, 1468–1478 (2019).
14. Zheng, Q. et al. Precise gene deletion and replacement using the CRISPR/Cas9 system in human cells. *Biotechniques* **57**, 115–124 (2014).
15. Cox, D. B., Platt, R. J. & Zhang, F. Therapeutic genome editing: prospects and challenges. *Nat. Med.* **21**, 121–131 (2015).
16. Liu, M. et al. Methodologies for improving HDR efficiency. *Front. Genet.* **9**, 691 (2018).
17. Anzalone, A. V. et al. Search-and-replace genome editing without double-strand breaks or donor DNA. *Nature* **576**, 149–157 (2019).
18. Matsoukas, I. G. Prime editing: genome editing for rare genetic diseases without double-strand breaks or donor DNA. *Front. Genet.* **11**, 528 (2020).
19. Liu, P. et al. Improved prime editors enable pathogenic allele correction and cancer modelling in adult mice. *Nat. Commun.* **12**, 2121 (2021).
20. Jang, H. et al. Prime editing enables precise genome editing in mouse liver and retina. Preprint at *bioRxiv* https://doi.org/10.1101/2021.01.08.425835 (2021).
21. Schene, I. F. et al. Prime editing for functional repair in patient-derived disease models. *Nat. Commun.* **11**, 5352 (2020).
22. Jiang, Y. Y. et al. Prime editing efficiently generates W542L and S621I double mutations in two ALS genes in maize. *Genome Biol.* **21**, 257 (2020).
23. Song, X., Huang, H., Xiong, Z., Ai, L. & Yang, S. CRISPR–Cas9^{D10A} nickase-assisted genome editing in *Lactobacillus casei*. *Appl. Environ. Microbiol.* **83**, 1259–1275 (2017).
24. Cho, S. W. et al. Analysis of off-target effects of CRISPR/Cas-derived RNA-guided endonucleases and nickases. *Genome Res.* **24**, 132–141 (2014).
25. Sfeir, A. & Symington, L. S. Microhomology-mediated end joining: a back-up survival mechanism or dedicated pathway? *Trends Biochem. Sci* **40**, 701–714 (2015).
26. Bhargava, R., Onyango, D. O. & Stark, J. M. Regulation of single-strand annealing and its role in genome maintenance. *Trends Genet.* **32**, 566–575 (2016).
27. Kim, H. K. et al. Predicting the efficiency of prime editing guide RNAs in human cells. *Nat. Biotechnol.* **39**, 198–206 (2021).
28. Mir, A. et al. Heavily and fully modified RNAs guide efficient SpyCas9-mediated genome editing. *Nat. Commun.* **9**, 2641 (2018).
29. Certo, M. T. et al. Tracking genome engineering outcome at individual DNA breakpoints. *Nat. Methods* **8**, 671–676 (2011).
30. Zhan, H., Li, A., Cai, Z., Huang, W. & Liu, Y. Improving transgene expression and CRISPR–Cas9 efficiency with molecular engineering-based molecules. *Clin. Transl Med.* **10**, e194 (2020).
31. Chen, R. et al. Enrichment of transiently transfected mesangial cells by cell sorting after cotransfection with GFP. *Am. J. Physiol.* **276**, F777–F785 (1999).
32. Homann, S. et al. A novel rapid and reproducible flow cytometric method for optimization of transfection efficiency in cells. *PLoS ONE* **12**, e0182941 (2017).
33. Pham, C. T., MacIvor, D. M., Hug, B. A., Heusel, J. W. & Ley, T. J. Long-range disruption of gene expression by a selectable marker cassette. *Proc. Natl Acad. Sci. USA* **93**, 13090–13095 (1996).
34. Grompe, M. et al. Loss of fumarylacetoacetate hydrolase is responsible for the neonatal hepatic dysfunction phenotype of lethal albino mice. *Genes Dev.* **7**, 2298–2307 (1993).
35. Paulk, N. K. et al. Adeno-associated virus gene repair corrects a mouse model of hereditary tyrosinemia in vivo. *Hepatology* **51**, 1200–1208 (2010).
36. Choi, J. et al. Precise genomic deletions using paired prime editing. *Nat. Biotechnol.* https://doi.org/10.1038/s41587-021-01025-z (in the press).
37. VanLith, C. J. et al. Ex vivo hepatocyte reprograming promotes homology-directed DNA repair to correct metabolic disease in mice after transplantation. *Hepatol. Commun.* **3**, 558–573 (2019).
38. Dutta, A. et al. Microhomology-mediated end joining is activated in irradiated human cells due to phosphorylation-dependent formation of the XRCC1 repair complex. *Nucleic Acids Res.* **45**, 2585–2599 (2016).
39. Aida, T. et al. Gene cassette knock-in in mammalian cells and zygotes by enhanced MMEJ. *BMC Genomics* **17**, 979 (2016).
40. Warby, S. C. et al. CAG expansion in the Huntington disease gene is associated with a specific and targetable predisposing haplogroup. *Am. J. Hum. Genet.* **84**, 351–366 (2009).
41. Wang, Y. et al. Identification of a Xist silencing domain by Tiling CRISPR. *Sci. Rep.* **9**, 2408 (2019).
42. He, W. et al. De novo identification of essential protein domains from CRISPR–Cas9 tiling-sgRNA knockout screens. *Nat. Commun.* **10**, 4541 (2019).

Methods

Cell culture and transfection. HEK293T cells (ATCC) and HEK293T-TLR cells[28,29] were maintained in Dulbecco's Modified Eagle's Medium (Corning) supplemented with 10% fetal bovine serum (Gibco) and 1% penicillin/streptomycin (Gibco). Cells were seeded at 70% confluence in a 12-well cell culture plate 1 d before transfection. PE-Cas9 (1.5 μg) and paired pegRNAs (1 μg; 0.5 μg each) were transfected with Lipofectamine 3000 reagent (Invitrogen).

pegRNA design and cloning. Sequences for pegRNAs are listed in Supplementary Table 1. Plasmids expressing pegRNAs were constructed by Gibson assembly using BsaI-digested acceptor plasmid (Addgene, 132777) as the vector.

Mouse experiments. All animal study protocols were approved by the UMass Medical School IACUC. *Fah*$^{\Delta Exon5}$ mice[34] were kept on 10 mg liter^{-1} NTBC water. Thirty micrograms of PE-Cas9 or Cas9 plasmid and 15 μg of paired pegRNA-expressing plasmids were injected into 9-week-old mice. One week later, NTBC-supplemented water was replaced with normal water, and mouse weight was measured every 2 d. As per our guidelines, when a mouse lost 20% of its body weight relative to the first day of measurement (the day when NTBC water was removed), the mouse was supplemented with NTBC water until the original body weight was achieved. After 40 d, mice were killed according to guidelines.

Immunohistochemistry. Portions of livers were fixed with 4% formalin, embedded in paraffin, sectioned at 5 μm and stained with hematoxylin and eosin for pathology. Liver sections were dewaxed, rehydrated and stained using standard immunohistochemistry protocols[43]. The anti-FAH (Abcam, 1:400) antibody was used. Images were captured using a Leica DMi8 microscope.

Genomic DNA extraction, amplification and digestion. To extract genomic DNA, HEK293T cells (3 d after transfection) were washed with PBS, pelleted and lysed with 50 μl of Quick extraction buffer (Epicenter) and incubated in a thermocycler (65 °C for 15 min and 98 °C for 5 min). A PureLink Genomic DNA Mini kit (Thermo Fisher) was used to extract genomic DNA from two different liver lobes (~10 mg each) per mouse. Target sequences were amplified using Phusion Flash PCR Master Mix (Thermo Fisher) with the primers listed in Supplementary Table 2. PCR products were analyzed by electrophoresis in a 1% agarose gel, and target amplicons were extracted using a DNA extraction kit (Qiagen). Ten nanograms of purified PCR products was incubated with I-SceI endonuclease (NEB) according to manufacturer's instructions. One hour after incubation, the product was visualized and analyzed by electrophoresis in 4–20% TBE gels (Thermo).

Tracking of indels by decomposition (TIDE) analysis to calculate indel rates at two cut sites. The sequences around the two cut sites of the target locus were amplified using Phusion Flash PCR Master Mix (Thermo Fisher) with the primers listed in Supplementary Table 2. Sanger sequencing was performed to sequence the purified PCR products, and the trace sequences were analyzed using TIDE software (https://tide.nki.nl/). The alignment window of the left boundary was set at 10 bp.

Quantification of total genomic DNA to determine the absolute editing rate of PEDAR. qPCR was used to calculate the absolute editing rate in total genomic DNA at the *HEK3* locus and was performed with SsoFast EvaGreen Supermix (Bio-Rad). Primers within the deletion region (P1 and P2), spanning the deletion region (P3 and P4) or across the deletion–insertion junction (P5 and P6) were designed (Supplementary Fig. 8a). Two 250-bp DNA fragments (referred to as WT and edited) of the same sequence with unedited or accurately edited target sites were designed and serially diluted and served as standard templates (Supplementary Fig. 8b). Using indicated primers and templates to perform qPCR, three standard curves were generated, reflecting the correlation between qPCR cycle number and the concentration of DNA without a 991-bp deletion (Supplementary Fig. 8c), with a 991-bp deletion (Supplementary Fig. 8d) or with an accurate 991-bp deletion/18-bp insertion (Supplementary Fig. 8e). Finally, three rounds of qPCR were performed using the edited genomic DNA as template and corresponding primer pairs (P1 + P2, P3 + P4 or P5 + P6). The standard curves were applied to calculate the absolute copy number of genomic DNA with deletion, without deletion or with accurate deletion–insertion.

The absolute rates of each type of editing introduced by PEDAR were calculated using the following equations: (1) accurate deletion–insertion editing rate = copy number of DNA with accurate deletion–insertion/copy number of DNA with and without deletion; (2) other deletion–insertion rate = (copy number of DNA with deletion − copy number of DNA with accurate deletion–insertion)/copy number of DNA with and without deletion; (3) absolute rate of small indels at two cut sites = copy number of DNA without deletion × indel rate at distinct cut site calculated by TIDE/copy number of DNA with and without deletion.

Flow cytometry analysis. To assess mCherry recovery rate, postediting HEK293T-TLR cells were trypsinized and analyzed using the MACSQuant VYB Flow Cytometer. Untreated HEK293T-TLR cells were used as a negative control for gating. To select cells with high transfection efficiency, 0.25 μg of GFP plasmid was cotransfected with PE-Cas9 and paired pegRNAs into TLR cells. Three days after transfection, cells were trypsinized and analyzed using the MACSQuant VYB flow cytometer. Cells transfected with GFP plasmid alone were used as a negative control for gating. Cells with a high expression level of GFP (~20% of the total population) were selected for analyzing mCherry signal. All data were analyzed using FlowJo 10.0 software.

High-throughput DNA sequencing of genomic DNA samples. Genomic sites of interest were amplified from genomic DNA using specific primers containing Illumina forward and reverse adaptors (listed in Supplementary Table 2). To quantify the percentage of desired deletion–insertions by PE-Cas9 or Cas9, we amplified the fragment containing deletions (~200 bp in length) from total genomic DNA to exclude length-dependent bias during PCR amplification. Twenty-microliter PCR 1 reactions were performed with forward and reverse primer (0.5 μM each), 1 μl of genomic DNA extract or 300 ng of purified genomic DNA and 10 μl of Phusion Flash PCR Master Mix (Thermo Fisher). PCR reactions were performed with the following parameters: 98 °C for 10 s, then 20 cycles of 98 °C for 1 s, 55 °C for 5 s and 72 °C for 10 s, followed by a final 72 °C extension for 3 min. After the first round of PCR, unique Illumina barcoding reverse primer was added to each sample in a secondary PCR reaction (PCR 2). Specifically, 20 μl of a PCR reaction contained 0.5 μM of unique reverse Illumina barcoding primer pair and 0.5 μM of common forward Illumina barcoding primer, 1 μl of unpurified PCR 1 reaction mixture and 10 μl of Phusion Flash PCR Master Mix. The barcoding PCR 2 reactions were performed with the following parameters: 98 °C for 10 s, then 20 cycles of 98 °C for 1 s, 60 °C for 5 s, and 72 °C for 10 s, followed by a final 72 °C extension for 3 min. PCR 2 products were purified by running on a 1% agarose gel using a QIAquick Gel Extraction kit (Qiagen) and eluting with 15 μl of Elution Buffer. DNA concentration was measured using a Bioanalyzer. DNA was sequenced on an Illumina MiSeq instrument (150 bp, paired-end) according to the manufacturer's protocols. Paired-end reads were merged with FLASh[44] (v1.2.11) with maximum overlap length equal to 150 bp. Alignment of amplicon sequence to the reference sequence was performed using CRISPResso2 (ref. [45]) (v2.0.32). To quantify accurate deletion–insertion edits, CRISPResso2 was run in HDR mode using the sequence with desired deletion–insertion editing as the reference sequence. The editing window was set to 15-bp. Editing yield was calculated as the number of HDR aligned reads/total aligned reads.

ClinVar data analysis. The ClinVar variant summary was obtained from the NCBI ClinVar database (accessed 31 December 2020). Variants with pathogenic significance were filtered by allele ID to remove duplicates. All pathogenic variants were categorized according to mutation type. The fractions of distinct mutation types were calculated using GraphPad Prism8.

Statistics and reproducibility. In Figs. 1c,d, 2b,c,f,g, 3d and 4f and Supplementary Figs. 2d,e, 3a,b,e,f, 4a,b and 5b,d, three biological replicates were performed with similar results. In Fig. 4c,e and Supplementary Fig. 6a, four mice (Fig. 4c, PE-Cas9, and Fig. 4e and Supplementary Fig. 6a) or two mice (Fig. 4c, Cas9) were used in the experiment with similar results.

Reporting Summary. Further information on research design is available in the Nature Research Reporting Summary linked to this article.

Data availability

A Reporting Summary for this article is available as a Supplementary Information file. The raw gel images underlying Figs. 1c,d, 2b,c,f,g, 3d and 4f and Supplementary Figs. 2d,e, 3a,b,e,f and 4a,b are provided as a Source Data file and an additional Supplementary Data file, respectively. The NCBI ClinVar database is accessible at https://www.ncbi.nlm.nih.gov/clinvar/. The raw DNA sequencing data are available at the NCBI Sequence Read Archive database under accession numbers PRJNA746292 and PRJNA746489. Source data are provided with this paper.

References

43. Xue, W. et al. Response and resistance to NF-κB inhibitors in mouse models of lung adenocarcinoma. *Cancer Discov.* **1**, 236–247 (2011).
44. Magoc, T. & Salzberg, S. L. FLASH: fast length adjustment of short reads to improve genome assemblies. *Bioinformatics* **27**, 2957–2963 (2011).
45. Clement, K. et al. CRISPResso2 provides accurate and rapid genome editing sequence analysis. *Nat. Biotechnol.* **37**, 224–226 (2019).

Acknowledgements

We thank C. Mello, P. Zamore, S. Wolfe, T. Flotte and E. Sontheimer for discussions and E. Haberlin for editing the manuscript. We thank E. Sontheimer (UMass Medical School) for providing the HEK293T-TLR cell line and M. Grompe (Oregon Health & Science University) for providing the *Fah*$^{\Delta Exon5}$ mice. We thank Y. Liu, Y. Gu and E. Kittler in the UMass Morphology, Flow Cytometry and Deep Sequencing Cores for support. W.X. was supported by grants from the National Institutes of Health (DP2HL137167, P01HL131471 and UG3HL147367), American Cancer Society (129056-RSG-16-093), the Lung Cancer Research Foundation and the Cystic Fibrosis Foundation. T.J. was supported by grants from National Institutes of Health (K99HL153940).

Author contributions

T.J. and W.X. designed the study. T.J. performed experiments. T.J., X.-O.Z. and Z.W. analyzed the data. T.J. and W.X. wrote the manuscript with comments from all authors.

Competing interests

UMass has filed a patent application on this work. W.X. is a consultant for the Cystic Fibrosis Foundation Therapeutics Lab. The other authors declare no competing interests.

Additional information

Supplementary information The online version contains supplementary material available at https://doi.org/10.1038/s41587-021-01026-y.

Correspondence and requests for materials should be addressed to Wen Xue.

Peer review information *Nature Biotechnology* thanks Daesik Kim and the other, anonymous, reviewer(s) for their contribution to the peer review of this work.

Reprints and permissions information is available at www.nature.com/reprints.

nature research

Corresponding author(s): Wen Xue

Last updated by author(s): 7/14/2021

Reporting Summary

Nature Research wishes to improve the reproducibility of the work that we publish. This form provides structure for consistency and transparency in reporting. For further information on Nature Research policies, see our Editorial Policies and the Editorial Policy Checklist.

Statistics

For all statistical analyses, confirm that the following items are present in the figure legend, table legend, main text, or Methods section.

n/a	Confirmed	
☐	☒	The exact sample size (*n*) for each experimental group/condition, given as a discrete number and unit of measurement
☐	☒	A statement on whether measurements were taken from distinct samples or whether the same sample was measured repeatedly
☐	☒	The statistical test(s) used AND whether they are one- or two-sided *Only common tests should be described solely by name; describe more complex techniques in the Methods section.*
☒	☐	A description of all covariates tested
☒	☐	A description of any assumptions or corrections, such as tests of normality and adjustment for multiple comparisons
☐	☒	A full description of the statistical parameters including central tendency (e.g. means) or other basic estimates (e.g. regression coefficient) AND variation (e.g. standard deviation) or associated estimates of uncertainty (e.g. confidence intervals)
☐	☒	For null hypothesis testing, the test statistic (e.g. *F*, *t*, *r*) with confidence intervals, effect sizes, degrees of freedom and *P* value noted *Give P values as exact values whenever suitable.*
☒	☐	For Bayesian analysis, information on the choice of priors and Markov chain Monte Carlo settings
☒	☐	For hierarchical and complex designs, identification of the appropriate level for tests and full reporting of outcomes
☒	☐	Estimates of effect sizes (e.g. Cohen's *d*, Pearson's *r*), indicating how they were calculated

Our web collection on statistics for biologists contains articles on many of the points above.

Software and code

Policy information about availability of computer code

Data collection	Illumina Miseq
Data analysis	CRISPResso V2.0.32 was used to analyze deep data for quantifying editing efficiency. FlowJo software V10 was used for flow cytometry analysis. Frequency, mean, and standard deviations were calculated using GraphPad Prism 8.

For manuscripts utilizing custom algorithms or software that are central to the research but not yet described in published literature, software must be made available to editors and reviewers. We strongly encourage code deposition in a community repository (e.g. GitHub). See the Nature Research guidelines for submitting code & software for further information.

Data

Policy information about availability of data

All manuscripts must include a data availability statement. This statement should provide the following information, where applicable:

- Accession codes, unique identifiers, or web links for publicly available datasets
- A list of figures that have associated raw data
- A description of any restrictions on data availability

A reporting summary for this article is available as a Supplementary Information file. The raw gel images underlying Figs. 1c-d, 2b–c, 2f-g, 3d,4f and Supplementary Figs. 2d-e, 3a-b, 3e-f, 4a-b are provided as a Source Data File and an additional supplementary data file, respectively. NCBI Clinvar database is accessible through the indicated link: https://www.ncbi.nlm.nih.gov/clinvar/. The raw DNA sequencing data are available at the NCBI Sequence Read Archive database under PRJNA746292 and PRJNA746489.

Field-specific reporting

Please select the one below that is the best fit for your research. If you are not sure, read the appropriate sections before making your selection.

☒ Life sciences ☐ Behavioural & social sciences ☐ Ecological, evolutionary & environmental sciences

For a reference copy of the document with all sections, see nature.com/documents/nr-reporting-summary-flat.pdf

Life sciences study design

All studies must disclose on these points even when the disclosure is negative.

Sample size	2x105 cells were used for editing in culture system. All cell samples were evaluated in at least biological triplicates (n = 3) to ensure the reproductability. Our previous editing studies have shown that this sample size and replications are sufficient to ensure reproducibility (Song et al, Nature Biomedical Engineering,2019 and Jiang et al, Nature Communications, 2020). For animal experiment, we described the size in the specific figure legend. The size is determined based on the availability of the mice and previous reports (Song et al, Nature Biomedical Engineering, 2019).
Data exclusions	No data was excluded.
Replication	All the culture-related experiments were done in biological triplicate in culture cells, n=3 ,on different days (every three days). All attempts at replication were successful, and standard deviations were in the expected ranges.
Randomization	After seeding cell into 12-well plate, we randomly decided which cells are for experiment group or control group. For mouse experiment, we randomly decide the mice treated for Cas9 or PE-Cas9 and for short or long-term studies.
Blinding	It is not applied to molecular and cell experiments. All mouse work are blind.

Reporting for specific materials, systems and methods

We require information from authors about some types of materials, experimental systems and methods used in many studies. Here, indicate whether each material, system or method listed is relevant to your study. If you are not sure if a list item applies to your research, read the appropriate section before selecting a response.

Materials & experimental systems

n/a	Involved in the study
☐	☒ Antibodies
☐	☒ Eukaryotic cell lines
☒	☐ Palaeontology and archaeology
☐	☒ Animals and other organisms
☒	☐ Human research participants
☒	☐ Clinical data
☒	☐ Dual use research of concern

Methods

n/a	Involved in the study
☒	☐ ChIP-seq
☐	☒ Flow cytometry
☒	☐ MRI-based neuroimaging

Antibodies

Antibodies used	Fumarylacetoacetate hydrolase antibody (ab83770, Abcam Inc), IHC 1:400
Validation	The specificity of the anti-Fah antibody has previously been confirmed (Yin et al, Nature Biotech, 2016).

Eukaryotic cell lines

Policy information about cell lines

Cell line source(s)	HEK293T cells and HEK293T-TLR cells
Authentication	HEK293T (ATCC) cells were valiated by supplier (ATCC) by STR analysis. And HEK293T-TLR cells were valiated using specific primers to amplify the inserted cassette. And the PCR products were analyzed by Sanger Sequencing.
Mycoplasma contamination	All cell lines tested negative for mycoplasma contamination
Commonly misidentified lines (See ICLAC register)	The cell lines used in this article are not in the list of misidentified lines.

Animals and other organisms

Policy information about studies involving animals; ARRIVE guidelines recommended for reporting animal research

Laboratory animals	FahΔExon5 mice was a mouse model of tyrosinemia. 9-week-old female mice were used in this study. Temperature of 65-75°F (~18-23°C) with 40-60% humidity are kept in the mouse room. A 14-hour light/10-hour dark cycle.
Wild animals	No wild animals were used in the study.
Field-collected samples	No field-collected samples were used in the study
Ethics oversight	All animal study protocols were approved by the UMass IACUC.

Note that full information on the approval of the study protocol must also be provided in the manuscript.

Flow Cytometry

Plots

Confirm that:

☒ The axis labels state the marker and fluorochrome used (e.g. CD4-FITC).

☒ The axis scales are clearly visible. Include numbers along axes only for bottom left plot of group (a 'group' is an analysis of identical markers).

☒ All plots are contour plots with outliers or pseudocolor plots.

☒ A numerical value for number of cells or percentage (with statistics) is provided.

Methodology

Sample preparation	Post-editing HEK293T-TLR cells were trypsinized, resuspended in 200ul PBS with 1% FBS, and directly analyzed by flow cytometry.
Instrument	mCherry analysis is analyzed by MACSQuant VYB Flow Cytometer. Sorting of mCherry positive cells was performed by BD FACS-Aira II.
Software	All data were analyzed by FlowJo10.0 software
Cell population abundance	mCherry positive rates w=mCherry positive cell number / total live cell number
Gating strategy	The cells were first gated based on FSC/SSC and FSCA/FSCH to select for live single cells. Unedited TLR cells were employed as negative control for gating mCherry signal.

☒ Tick this box to confirm that a figure exemplifying the gating strategy is provided in the Supplementary Information.